Geophysical Journal International

Geophys. J. Int. (2024) **238,** 783–793
Advance Access publication 2024 May 31
GJI Seismology

https://doi.org/10.1093/gji/ggae188

Gradient-based joint inversion of point-source moment tensor and station-specific time-shifts

Thanh-Son Phạm

Research School of Earth Sciences, The Australian National University, Canberra, Acton, ACT 0200*, Australia. E-mail: thanhson.pham@anu.edu.au*

Accepted 2024 May 28. Received 2024 May 20; in original form 2023 September 16

SUMMARY

The misalignment of the observation and predicted waveforms in regional moment tensor inversion is mainly due to seismic models' incomplete representation of the Earth's heterogeneities. Current moment tensor inversion techniques, allowing station-specific time-shifts to account for the model error, are computationally expensive. Here, we propose a gradient-based method to jointly invert moment-tensor parameters, centroid depth and unknown station-specific time-shifts utilizing the modern functionalities in deep learning frameworks. A L_2^2 misfit function between predicted synthetic and time-shifted observed seismograms is defined in the spectral domain, which is differentiable to all unknowns. The inverse problem is solved by minimizing the misfit function with a gradient descent algorithm. The method's feasibility, robustness and scalability are demonstrated using synthetic experiments and real earthquake data in the Long Valley Caldera, California. This work presents an example of fresh opportunities to apply advanced computational infrastructures developed in deep learning to geophysical problems.

Key words: joint inversion; Computational seismology; Theoretical seismology; Moment tensor; Optimization.

1 INTRODUCTION

A seismic moment tensor (MT) is a mathematical representation of a seismic source under the point-source assumption in space and time when wavelengths are several times longer than the fault geometry (Aki & Richards 2002). A full MT is a 3×3 matrix, but the net torque is negligible for most underground earthquakes, and the matrix is symmetric with six unknown elements (e.g. Jost & Herrmann 1989; Stein & Wysession 2003). In this study, we use the northeast–down coordinate system for an MT, denoted as,

$$m = [m_k;\ k = 1 \dots 6] = [m_{nn},\ m_{ee},\ m_{dd},\ m_{ne},\ m_{nd},\ m_{ed}] \in R^6. \quad (1)$$

In MT inversion, a set of Green's functions (GFs), or Earth's structure responses, $G_k(\xi,\ x,\ t)$, is computed in advance for six orthogonal bases of the MT space, in which, ξ and x are the source and receiver locations. Then, a tensor (linear) multiplication predicts the observed waveforms,

$$d(t) = m \cdot G(\xi,\ x,\ t) = \sum_k m_k\, G_k. \quad (2)$$

$G \in R^{n_r \times n_c \times 6 \times n_t}$ is a forth-order tensor and $d \in R^{n_r \times n_c \times n_t}$ is a third-order tensor, where n_r, n_c and n_t are number of receivers, number of components in each receiver and number of samples, respectively. The MT solution, m^*, can be approximated by its least-square estimate of the linear system,

$$m^* = d \cdot G^T \cdot \left(G \cdot G^T\right)^{-1}. \quad (3)$$

The superscript T denotes the matrix transposition.

However, in practice, the numerical predictions and observed waveforms are often not aligned (Figs 1a and b), and the misalignment could severely affect the MT solution estimate (Zhao & Helmberger 1994; Zhu & Helmberger 1996). Let τ be an unknown station-specific time-shift to align the observation to the prediction, and eq. (2) can be rewritten as,

$$d(t - \tau) = m \cdot G^h(t). \quad (4)$$

From eq. (4), for clarity, we drop the source, ξ, and receiver, x, locations as they are assumingly known in this study, but the centroid depth, h, is superscripted because it is considered an inversion parameter.

The first contribution to the misalignment, τ, is due to the error in the event's origin time. This leads to a baseline time-shift applied to all stations' waveforms to best match the synthetic prediction. Secondly, the lack of complete knowledge of the Earth's structures results in path-specific time-shifts (Zhao & Helmberger 1994; Zhu & Helmberger 1996; Zhu & Ben-Zion 2013; Silwal & Tape 2016). Indeed, a 1-D velocity model is often used in regional surface wave inversion. If the model is faster or slower than the real Earth along the path toward a receiver, the observed waveform needs to be shifted backward or forward to account for the structural error. The presence of unknown station-specific time-shifts makes the MT inversion strongly non-linear, whose existing computational methods are computationally expensive.

Indeed, the cut-and-paste (CAP) algorithm (Zhao & Helmberger 1994; Zhu & Helmberger 1996) and its variation (Zhu &

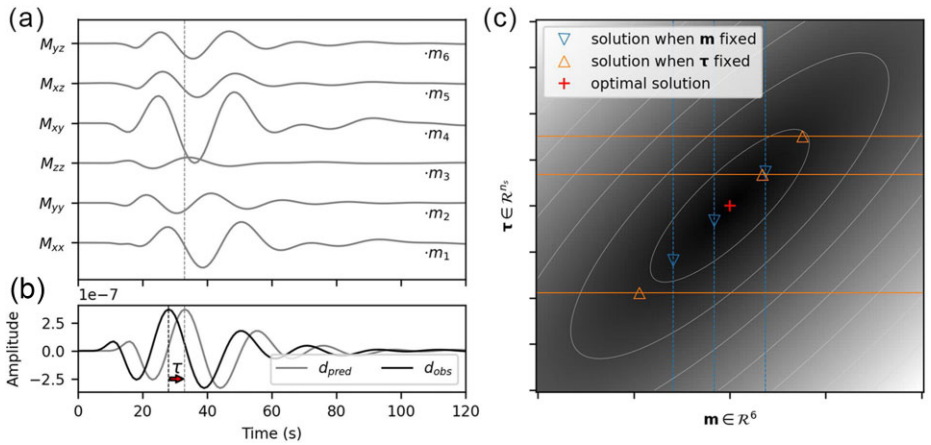

Figure 1. Motivating problem for joint inversion of moment tensor (MT) parameters, m, and unknown station-specific time-shifts, τ. (a) The waveforms are Green's functions corresponding to elementary MTs, M_i, $i = 1, \ldots, 6$. (b) The typical mismatch between observed and predicted waveforms. The observed waveform, d_{obs}, needs to be shifted by an unknown time-shift, τ, to match the predicted waveform, d_{pred}. (c) Schematic demonstration of a global minimum in the joint parameter space of MT parameters and station-specific time-shifts, m and τ. Horizontal and vertical-coloured lines represent two widely used approaches for MT inversion with unknown time-shifts. The vertical lines sketch the idea behind the cut-and-paste method (Zhao & Helmberger 1994; Zhu & Helmberger 1996), while the horizontal lines sketch the idea behind the time domain MT method (Dreger *et al.* 2000). Here we consider full MT solutions, so $m \in R^6$, and one time-shift for each station, so $\tau \in R^{n_r}$, where n_r is the number of seismic stations.

Ben-Zion 2013) are widely used for regional full-waveform MT inversion, where time-shifts are allowed to account for model errors. In this algorithm, a misfit value is computed for an imputed MT solution, assuming the optimal alignment between predicted and observed waveforms can be determined by cross-correlation (depicted by vertical blue lines in Fig. 1c). Then, the best MT solution is grid-searched as the smallest misfit over the entire parameter MT space, which often results in a costly computational burden. For example, Silwal & Tape (2016) and Alvizuri & Tape (2018) recently implemented this approach for full MT inversion using a uniform parametrization of MT space (Tape & Tape 2015). The grid search was implemented on a cluster due to the computational scale (Alvizuri & Tape 2018; Thurin *et al.* 2022) given that 20 million trials were evaluated for each earthquake.

Alternatively, an MT solution can be solved efficiently using least-square estimation given an imputed set of station-specific time-shifts (depicted by horizontal orange lines in Fig. 1c). After marching the grid of all possible combinations of station-specific time-shifts, the optimal MT solution corresponds to the minimum misfit (e.g. Dreger *et al.* 2000). More recently, Hejrani *et al.* (2017) assumed a single time-shift for all stations to account for possible errors in the catalogued centroid time. The grid search for station-specific time-shifts is also costly due to the exponentially larger number of combinations to explore, especially when the analysis involves a larger number (i.e. more than 10) of stations.

The ensemble sampling method in the Bayesian framework in the joint space of MT parameters and unknown time-shifts (Viltres *et al.* 2021; Hu *et al.* 2023) is a relatively independent approach of the above-mentioned approaches. This approach has recently become possible thanks to the advance of powerful probabilistic sampling methods (Roberts & Rosenthal 2001; Del Moral *et al.* 2006; Goodman & Weare 2010). It narrows the targeted sampling near the optimal solution, which provides a useful estimate of the parameters' uncertainty. Most recently, Thurin & Tape (2023) used a gradient-free search, that is the covariance matrix adaptation–evolution strategy (CMA-ES), for an optimal fit of possible source mechanism's parameters, which are three for a single force or six for a full MT, and a time-shift accounting for origin time error. However, the gradient-free approaches also require millions of misfit evaluations (Hu *et al.* 2023; Thurin & Tape 2023) and suffer a severe scalability problem when considering station-specific time-shifts. If n_r stations are used simultaneously in the inversion and a time-shift is assumed for each station, the dimension of the unknown space, $6 + n_r$, grows, while the MT parameters occupy just a small subspace.

This study proposes a gradient-based method in the optimization framework to tackle the non-linear inverse problem. Note that the gradient-based iterative method dates back to the early development of the global centroid MT inversion (Dziewonski *et al.* 1981), which searches for nine unknowns, including the deviatoric MT solution, centroid time and hypocentral coordinates. Recent studies have embraced comprehensive but computationally demanding treatments of the parameters, and more including source time function parametrizations, with uncertainty estimates for earthquake sources at local (Kühn *et al.* 2020), regional (Vasyura-Bathke *et al.* 2020; Petersen *et al.* 2021) and global scales (Stähler & Sigloch 2014). On the other hand, there is an emerging class of deep-learning-based methods (Steinberg *et al.* 2021; Nooshiri *et al.* 2022) for determining the MT and hypocentral parameters with their associated uncertainties. The approach is computationally demanding in the training phase, often on synthetic training datasets, but fast in evaluating results in the production phase. This paper contributes to the wide MT inversion methodological spectrum by providing a new method that carefully treats station-specific time-shifts as a proxy to incorporate 3-D structural heterogeneities in the inversion at a reasonable computational cost.

The remainder of this paper is structured as follows. First, we represent the misfit function between the prediction and time-shifted observation in the spectral domain, where the misfit is differentiable to all dependent parameters, including MT parameters, centroid depth and station-specific time-shifts. Consequently, the misfit function can be minimized using a gradient descent algorithm to obtain an optimal solution. The algorithm is implemented in *TensorFlow*, a popular deep-learning framework, to utilize its advanced autodifferentiation functionality and computational performance. The method's feasibility, robustness and scalability are benchmarked in carefully designed synthetic experiments and real data events in the Long Valley Caldera region.

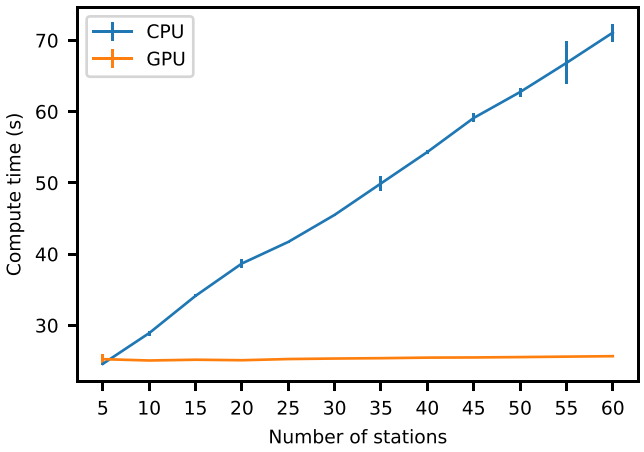

Figure 2. Computational scalability of the inversion method. Blue and orange lines show the computing times after 1000 epochs on a Central Processing Unit (CPU) and a Graphical Processing Unit (GPU) of the Australian National Computing Infrastructure's Gadi cluster as functions of the number of stations involved in the inversion. The error bars show the 1σ runtime variation in 10 independent repetitions.

2 METHODOLOGY

2.1 Data preparation and pre-processing

Seismic waveforms and station metadata were downloaded from the North California Earthquake Data Center (NCEDC). The retrieved waveforms were corrected for instrumental responses for velocity seismograms, then filtered between 20 and 50 s, with an acausal, 4-corner Butterworth bandpass filter and down-sampled to 1 sample per second. We visually inspected the pre-processed waveforms and eliminated those having glitches or exhibiting anomalously high noise levels. They were then arranged into a 3-D tensor in $R^{n_r \times n_c \times n_t}$, where n_r, $n_c = 3$, and n_t are the numbers of receivers, channels and time samples. In this study, all waveforms are 250 s long (i.e. $n_t = 250$) starting from the origin time reported in the NCEDC catalogue.

2.2 Calculation of GFs

Synthetic velocity seismograms of an impulse source corresponding to six orthogonal MT bases were generated using the frequency-wave number method in the *Computer Program in Seismology* package (Herrmann 2013). We used the 1-D South California model (Dreger & Helmberger 1990), which is later referred to as the SoCal model, like previous studies of earthquakes in the region (Dreger *et al.* 2000; Minson & Dreger 2008). The calculated seismograms are filtered and resampled in the same way as the observed data and arranged into a 4-D tensor $G \in R^{n_s \times n_c \times n_e \times n_t}$ and $n_e = 6$ is the number of MT orthogonal bases.

To rapidly generate GF at an arbitrary depth, h, we first computed an array of GFs over regular discrete depths, for example at every 2 km. The GF at an arbitrary depth, h, is linearly interpolated from the pre-computed GFs at adjacent depth grids, h_k and h_{k+1},

$$G^h(t) = \frac{h_{k+1} - h}{h_{k+1} - h_k} G^{h_k}(t) + \frac{h - h_k}{h_{k+1} - h_k} G^{h_{k+1}}(t). \tag{5}$$

As demonstrated later, the linear interpolation is sufficient to evaluate GF as a continuous function of the depth. A more sophisticated interpolation scheme has been used to interpolate GFs as a function of the 3-D epicentral coordinates (Simutė *et al.* 2023).

2.3 Differentiable misfit function and optimized inversion

Without losing the generality, we consider the inverse problem with an unknown time-shift, τ, for a single observed seismogram. An L_2^2 misfit function between predicted and shifted (or translated) observed waveforms is defined as,

$$J(m, \tau) = \int_t \left| m \cdot G^h(t) - d(t - \tau) \right|^2 dt. \tag{6}$$

The integration over time is a notional representation of the summation over discrete digital waveform samples.

A time-shifted function in the time domain is a multiplication in the frequency domain, f, via a Fourier transform,

$$F\{d(t - \tau)\}(f) = F\{d(t)\}(f) \exp(-i\omega\tau), \tag{7}$$

where $\omega = 2\pi f$. The Fourier transform of the integral kernel in eq. (6) becomes,

$$F\left\{m \cdot G^h(t) - d(t - \tau)\right\}(f) = F\left\{m \cdot G^h(t)\right\}(f) - F\{d(t)\}(f) \exp(-i\omega\tau). \tag{8}$$

For convenience, we denote $\widehat{G^h} := F\{G^h(t)\}(f)$, $\hat{d} := F\{d(t)\}(f)$. Because the L_2^2 norms in spectral and temporal domains equal (i.e. Parseval's theorem–Gradshteyn *et al.* 2000), the misfit function, eq. (6), can be rewritten in the spectral domain as

$$J(m, \tau, h) = \int_f \left| m \cdot \widehat{G^h} - \hat{d} \exp(-i\omega\tau) \right|^2 df. \tag{9}$$

In eq. (9), $|\cdot|$ is the absolute value of the complex spectra, so the cost function, $J(m, \tau, h)$, is continuous and differentiable to all dependent variables, m, τ and h, indeed,

$$\frac{\partial J}{\partial m} = 2 \int_f \left(\widehat{G^h}_r \cdot \hat{D}_r + \widehat{G^h}_i \cdot \hat{D}_i \right) df, \tag{10}$$

$$\frac{\partial J}{\partial \tau} = 2\omega \int_f \left[\hat{D}_r \cdot \left(\hat{d}_i \cos\omega\tau - \hat{d}_r \sin\omega\tau \right) + \hat{D}_i \cdot \left(\hat{d}_i \cos\omega\tau + \hat{d}_r \sin\omega\tau \right) \right] df, \tag{11}$$

$$\frac{\partial J}{\partial h} = \int_f 2 \left(\frac{G_r^{h_{k+1}} - G_r^{h_k}}{h_{k+1} - h_k} \cdot m \cdot D_r + \frac{G_i^{h_{k+1}} - G_i^{h_k}}{h_{k+1} - h_k} \cdot m \cdot D_i \right) df, \tag{12}$$

where

$$\begin{aligned} D_r &:= \left(m \cdot \widehat{G^h}_r - \hat{d}_r \cos\omega\tau - \hat{d}_i \sin\omega\tau \right) \\ D_i &:= \left(m \cdot \widehat{G^h}_i - \hat{d}_i \cos\omega\tau + \hat{d}_r \sin\omega\tau \right). \end{aligned} \tag{13}$$

D denotes the difference of the spectra of the observed and predicted waveforms in the integral kernel in eq. (9). Subscripts i, r denote the real and imaginary components of the Fourier transforms of Green's tensor and observed data. With the differentiable misfit function, a gradient descent algorithm can derive the optimum corresponding to the inverse solution in the joint space of MT parameters, centroid depth and time-shift.

In this work, we assume a single time-shift for all three components of one station to demonstrate the method's feasibility. By assuming so, we ignore the Earth's structure anisotropy, which could result in different time-shifts in surface wave arrivals in radial and tangential seismograms. The time-shifts are a proxy for isotropic heterogeneity in 3-D Earth structures when approximated by 1-D velocity models (Zhao & Helmberger 1994; Zhu & Helmberger 1996; Zhu & Ben-Zion 2013). Thus, our inversion has n_r time-shifts, earthquake depth and 6 MT parameters as unknowns.

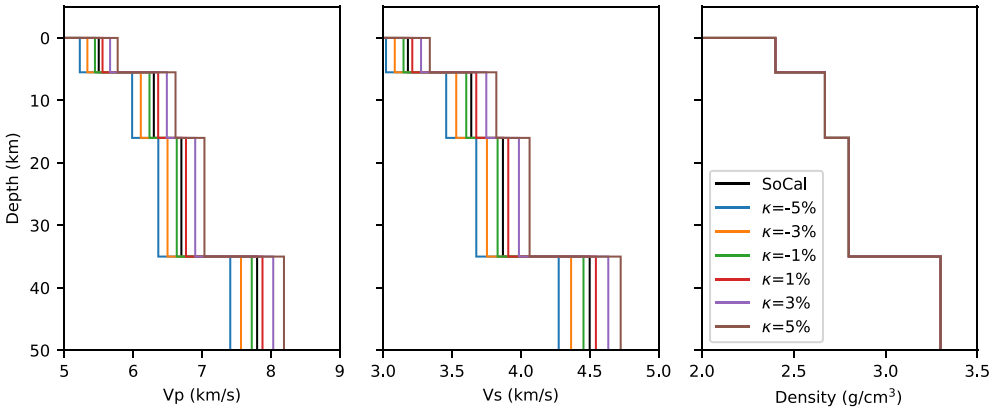

Figure 3. Earth models are used in synthetic experiments. The back lines show the South California (SoCal) model (Dreger & Helmberger 1990) and the coloured lines plot perturbed models with $\kappa = \pm 1$ per cent, ± 3 per cent and ± 5 per cent from the original *P*- and *S*-wave speeds in all layers.

2.4 Algorithm implementation and uncertainty estimation

Our implementation utilizes the auto differentiation functionality available on *TensorFlow* (*www.tensorflow.org*), a popular deep learning framework. The partial derivatives, eqs (10)–(12), can be automatically calculated by backpropagating the loss function defined in eq. (9). The deep learning framework also offers well-tested, high-performance gradient descent algorithms, such as Adam (Kingma & Ba 2014). In the present implementation, we use the Adam optimizer as a default option due to its empirical performance. As demonstrated later, the implementation enables acceleration on a graphic processing unit (GPU), resulting in excellent scalability to data size with a negligible increase in computing time. As we utilize the core functions of a modern deep learning framework, the inversion algorithm can also be implemented in other frameworks with similar functionalities, such as *PyTorch*, as the developers prefer.

Because the event's magnitude is on a logarithmic scale but generally unknown, the amplitudes of observed seismograms and precomputed GFs can be in largely different dynamic ranges. This is an inherent challenge for iterative algorithms because the initial solution must be relatively close to the optimum to guarantee the algorithm's convergence. Here, we normalize the observation and Green's tensor with their absolute medians to reduce the logarithmic magnitude scaling difference. The actual magnitude of the MT solution will be restored afterward using the ratio between the median values. When waveform amplitudes are normalized in this way, we empirically found a learning rate of 0.2, or similar values in the same magnitude order, performs well for the examples presented in this paper. The learning rate defines the relative step length when descending along the gradient direction.

Another important aspect is the proposed method's excellent scalability to tens of seismic stations. Fig. 2 features the compute time of the algorithm on a single central processing unit (CPU) and a single graphical processing unit (GPU) on the Australian National Computational Infrastructure's Gadi cluster for test runs with an increasing number of seismic stations, n_r. To fairly compare the running time, we terminated all inversions at 1000 epochs without considering the actual convergence of the MT solutions. When running on a CPU, the compute time increases less than three times given that the input size was increased 12 times. This indicates the CPU code's strong sublinear scalability. The run time is even faster on a GPU, yet, more significantly, the input size increase does not affect the compute time. This starkly contrasts with existing methods, as discussed in the Introduction, whose efficacy depends strongly on the input sizes.

To estimate the uncertainties of the recovered parameters, we repeated the inversion in 96 independent runs with different initial solutions, thanks to the inversion's efficiency. To minimize the risk of local minima solutions, we select 50 per cent solutions corresponding to the smallest losses, which almost always converge to the global minimum. We use their mean and one standard deviation to appraise the final estimates of the MT solutions, epicentral depth, station-specific time-shifts and their uncertainties. On a practical note, despite the better runtime of the GPU version (Fig. 2), we prefer to execute the CPU inversion in embarrassing parallel on 48 cores of a single node on the Gadi cluster, which results in an overall better runtime.

3 SYNTHETIC EXPERIMENTS

This section demonstrates the method in a series of controlled numerical experiments. The experiments utilize velocity models slightly perturbed from the SoCal model (Dreger & Helmberger 1990) to generate synthetic data, while the original model is used in the inversion to recover the MT solutions. Fig. 3 shows an array of perturbed earth models, where *P*- and *S*-wave speeds in all layers are increased or decreased by $\kappa = \pm 1$ per cent, ± 3 per cent and ± 5 per cent from their original values. The source-station configuration is similar to the M_w 4.9, 1997/11/22 17:20:35 event, featured later in Section 4.1. The input MT, fixed at 10 km depth, is highly non-DC, consisting of 30 per cent negative isotropic, 35 per cent double couple and 35 per cent CLVD components. Synthetic data are filtered in 20–50 s and then added with white noise with a standard deviation equal to 10 per cent of the original signals' standard deviation.

Fig. 4 presents the exemplary inversion results when the earth model is perturbed by $\kappa = -3$ per cent. Results for the correct model and other perturbation values are shown in Figs S1–S6. Given that the SoCal model is inaccurate in this example, recovered MT solutions and source depths are sufficiently close, though not exact, to the truth values, which confirms the method's capacity. Because 1σ errors estimated from 50 per cent best solutions for all parameters, the ISO/DC/CLVD decomposition components, event depth and station-specific time-shifts are small, the method can be

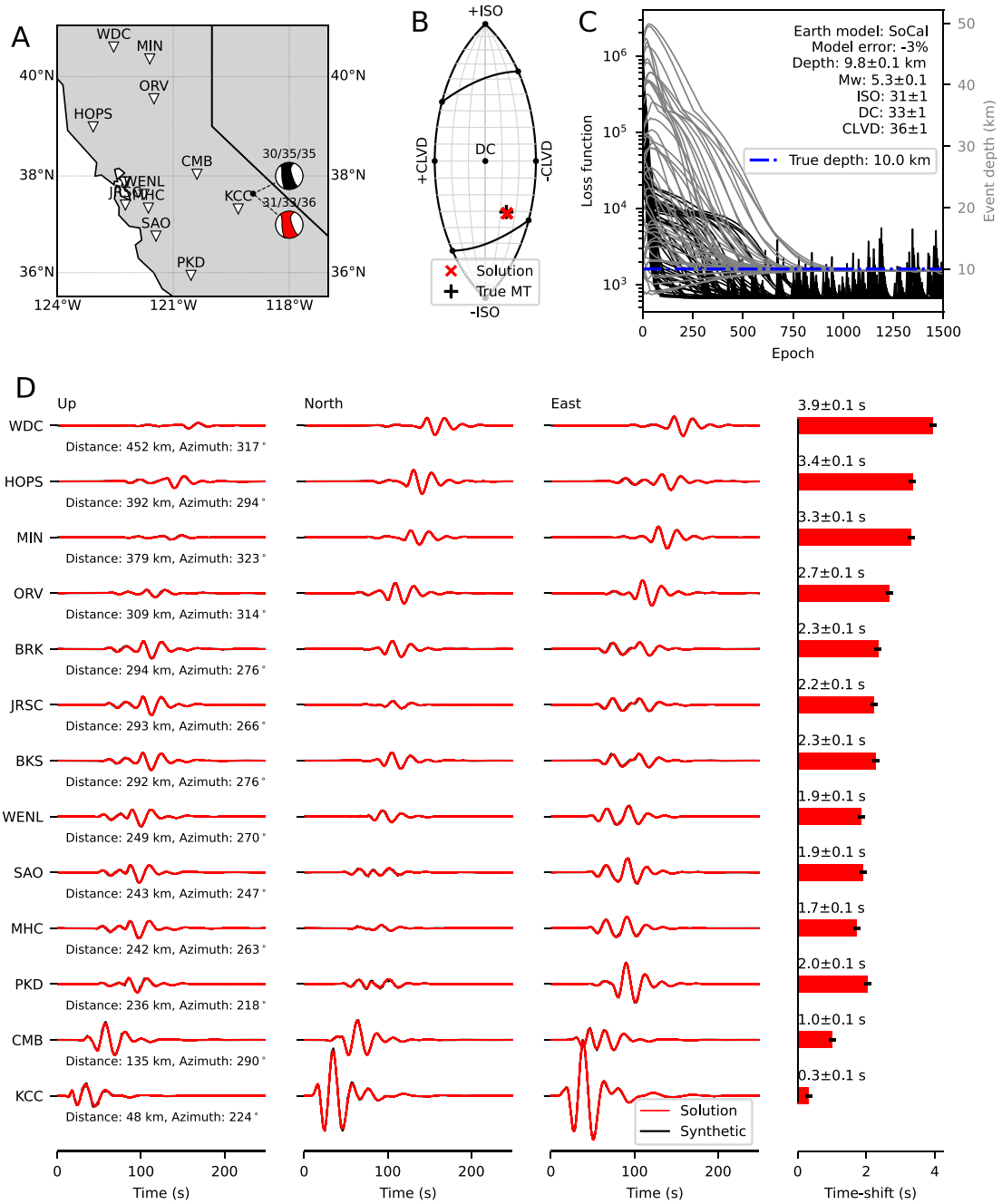

Figure 4. Summary of inversion results for a synthetic experiment using data from an incorrect earth model, that is $\kappa = -3$ per cent. The centroid depth is fixed at 10 km. (a) Source-station location map. Black and red beach balls show the deviatoric moment tensors (MT) of the actual input and the recovered solution. (b) The input (black plus) and recovered MTs (red cross) are marked on a lune diagram (Tape & Tape 2012). (C) Black lines show the evolution of descending losses (eq. 9) as a function of epochs for 48 solutions having the smallest losses out of the 96 independent runs. Grey lines plot the corresponding centroid-depth evolutions. The text denotes the forward earth model, model error magnitude, recovered event depth, moment magnitude and standard decomposition of isotropic (ISO), double couple (DC) and compensated linear vector dipole (CLVD) percentages. (d) Synthetic data and 48 best-predicted waveforms are shown in black and red, respectively. The right panel shows the output station-specific time-shifts and estimated uncertainties.

considered highly precise. However, the method's precision should be distinguished by its accuracy, representing the recovered solution's closeness to the true input. The inversion accuracy is subjected to the forward problem's quality, subject to the imposed model errors, so the small inversion inaccuracy is unavoidable. As summarized in Figs 5(a) and (b), it is encouraging our proposed method, accounting for structural errors by station-specific time-shifts, effectively recovers the input MT at reasonable accuracy.

Lastly, Fig. 5(c) shows the remarkable correlation between the trend of station-specific time-shifts recovered by the inversion and the imposed earth model errors. When model errors are negative, the original model, SoCal, is faster than the synthetic Earth structures (refer to Fig. 3). Hence, surface wave trains predicted by the SoCal model arrive earlier than those in the synthesized data. Consequently, negative time-shifts are required to shift the synthetic observation backward to match the forward prediction. In

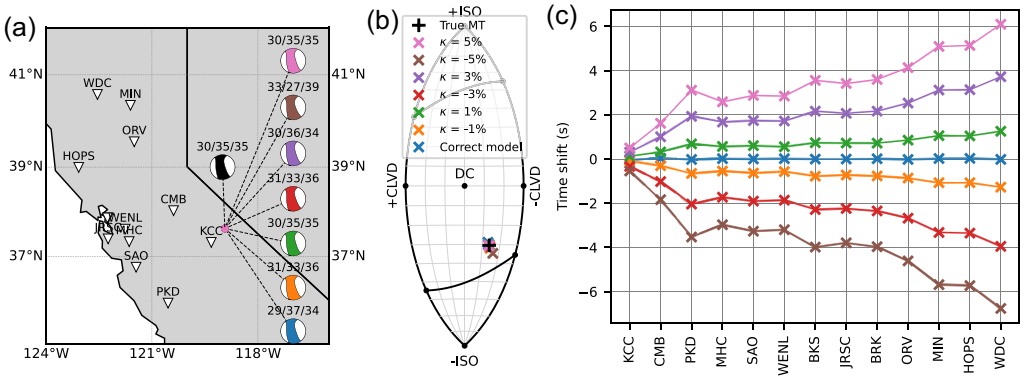

Figure 5. Station-specific time-shifts recovered as functions of Earth model errors in synthetic experiments. The colour codes in the legend of panel (b) denote the results in all panels. (a) Source-station location map used in the synthetic experiments. The earthquake is fixed at 10 km depth. The black beach ball plots the deviatoric mechanism of the input MT, and the coloured beachballs plot the recovered MTs inverting synthetic data from perturbed earth models. (b) The input and recovered MT solutions are plotted on a lune diagram (Tape & Tape 2012). (c) This panel plots the trends of recovered station-specific time-shifts sorted with increasing epicentral distances.

general, the shift amounts needed to increase with epicentral distances, so a negative model error corresponds to a decreasing trend of recovered time-shifts. On the other hand, a positive model error corresponds to increasing time-shifts relative to distances. This observation suggests one can compare the earth model relative to the actual structures if simplistically assuming an azimuthally homogenous structure in the region.

4 RESULTS

4.1 M_w 4.9, 1997/11/22 17:20:35, Long Valley Caldera volcanic event

We use data from a previously studied, non-double-couple event in the Long Valley Caldera (M_w 4.9, 1997/11/22 17:20:35) to further demonstrate the feasibility and robustness of the proposed inversion method. This event, often referred to as LV2, was in a sequence of large events during the volcanic unrest from 1997 to 1999 (Dreger *et al.* 2000; Minson & Dreger 2008; Phạm & Tkalčić 2021). Broad-band seismic data were retrieved from 13 broad-band seismic stations of the Berkeley Digital Seismograph Network (Fig. 6a) and filtered between 20 and 50 s. As noted above, an array of GFs is computed for every 2 km down to 50 km depth for the same source-station configuration, from which GF at an arbitrary depth can be linearly interpolated.

Fig. 6 summarizes the inversion result from real data for this event. Like the synthetic data examples, the real data inversions are also repeated 96 times independently, and only half of the solutions with the smallest losses are selected to compute the mean solution and 1σ uncertainties. The recovered MT solution has a dominant double couple (DC) 57 $\pm$ 1 per cent, large isotropic (ISO) 33 $\pm$ 1 per cent and compensated linear dipole (CLVD) 9 $\pm$ 1 per cent components (Fig. 6b). This event's estimated source depth is highly confident at 10.1 $\pm$ 0.1 km, which is deeper than 5.1 km reported in the NCEDC catalogue. Predicted waveforms corresponding to the selected solutions exhibit good fits with observed waveforms after time-shifted (Fig. 6d).

To further examine the robustness of the recovered solution, we repeat the complete inversion procedure for multiple subsets of 5, 7, 9 and 11 stations drawn from the original set of 13. The complete inversion procedure was repeated for seven different realizations of each subset size. In each subset realization, a seismic station was selected randomly without repetition until the size was reached. The probability of picking a station is inversely proportional to its distance to the earthquake source; in other words, a station closer to the source is more likely to be picked. As a result, seven solutions correspond to crosses in each colour in all panels of Fig. 7.

The source types of 28 recovered MT solutions with the station subsets are distributed closely around the reference solution, recovered with all 13 stations (Fig. 7a). Besides the non-DC source types, the DC parts of the full MT solutions can also be constrained reasonably well with the station subsets (Fig. 7b). Indeed, the Kagan angles, being the smallest angle to match the subset solutions' DC to the reference's DC parts (Kagan 1991), are always smaller than 10°. Furthermore, the angles generally decrease when more stations are included in the inversions because more stations yield better azimuthal coverage, thus better constraining the DC components. Lastly, Fig. 7(c) features the consistency of the recovered time-shifts among the station subsets, which is discussed in the following section.

The presence of the significant CLVD component in the MT solution of this event (Figs 6b and 7a) confirms the findings by Phạm & Tkalčić (2021). It is worth noting that both studies considered the effects of Earth's structural error using different approaches. The previous study considered the influence of the 1-D velocity model's error by simulating synthetic waveforms and their covariance matrices. This study, however, utilizes station-specific time-shifts as a proxy to tolerate earth model error, which largely results in waveform misalignment (Hu *et al.* 2023). The agreement of a significant CLVD component for this event, which was overlooked in the past (Phạm & Tkalčić 2021), revealed by two different approaches, corroborates the importance of properly treating the earth model's error in MT inversion methods.

4.2 Robustness of recovered station-specific time-shifts

Given that the previous section features the robustness of resolving MT parameters, this section demonstrates the robustness of the recovered time-shifts. First, we note that the time-shifts for multiple station subsets for event M_w 4.9, 1997/11/22 17:20:35, presented in the previous section, are highly consistent except for stations MIN and WDC. The large variations in time-shifts at the two stations

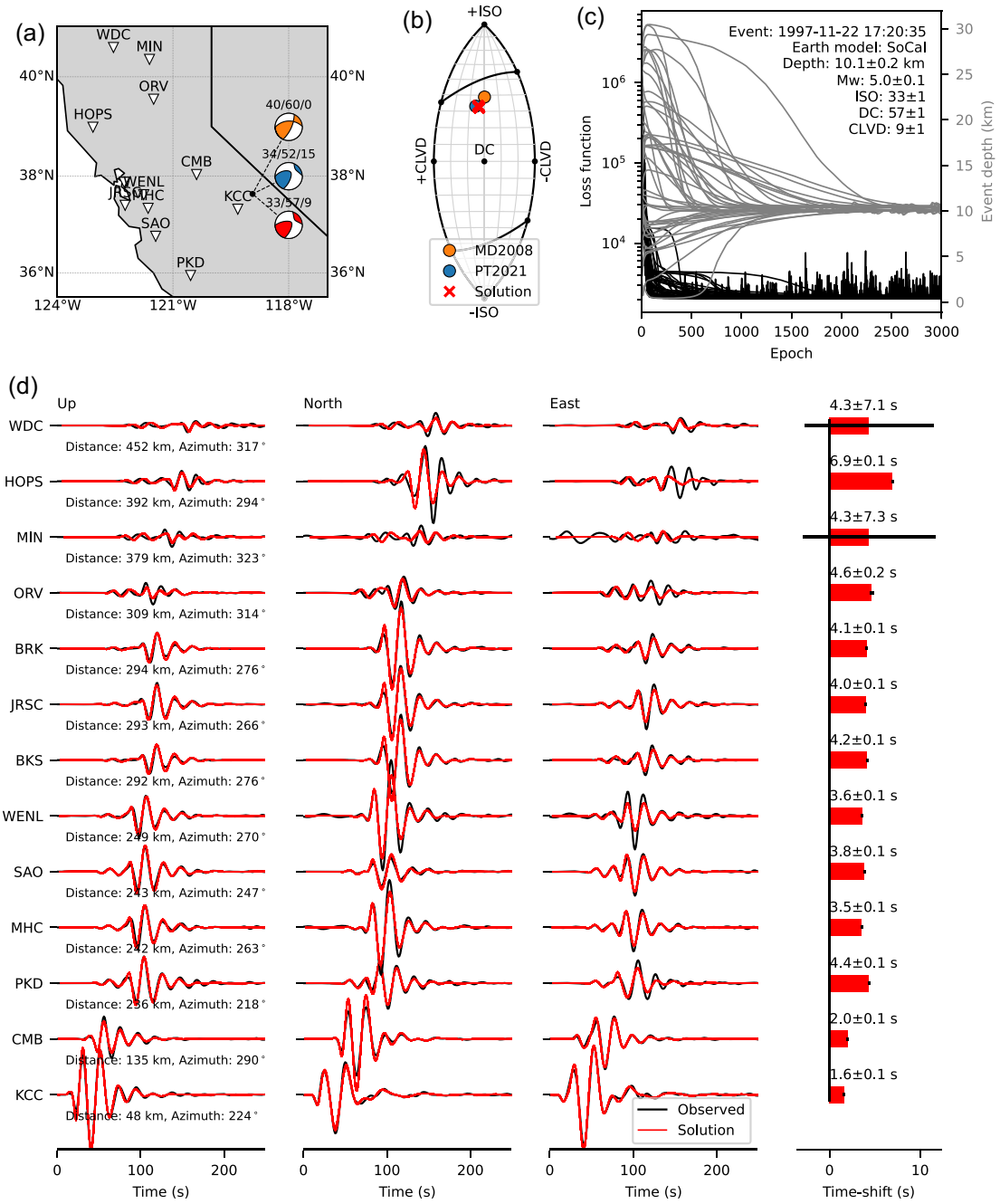

Figure 6. Summary of inversion results for real data computed from 1997/11/22 17:20:35 event catalogued in the North California Earthquake Data Center (NCEDC). The following colour codes are used for solutions of previous work: orange for MD2008 (Minson & Dreger 2008) and blue for PT2021 (Phạm & Tkalčić 2021). Other details are the same as in Fig. 4.

are likely due to their small waveform amplitudes (in comparison with station HOPS of a similar epicentral distance), which results in a low signal-to-noise ratio. The same reason also causes the large uncertainties in these stations' time-shifts inverted for all 13 stations (Fig. 6d).

Furthermore, we retrieve data from six events in Long Valley Caldera's 1997–1999 unrest sequence (Fig. 8a). A set of 13 stations recording all six events is used for the inversion to compare relative variation in time-shifts (Fig. 8c). The selected events show a wide variety of source types (Fig. 8b). Five events in the caldera's closest vicinity exhibit significant non-DC components, which are likely related to volcanic activities. The only event in the Nevada site is DC-dominant, likely due to its tectonic nature.

Despite the diversity in source types, the recovered station-specific time-shifts show a common decreasing trend relative to epicentral distances among all six events (Fig. 8c). Similar to event 1997/11/22 17:20:35 noted above (Fig. 6d), time-shifts recovered for stations MIN and WDC of event 1999/05/15 13:22:10 (Fig. S11D) are also largely uncertain due their characteristic waveform amplitudes are much lower compared to adjacent stations. We note that the absolute station-specific time-shifts are subjected to uncertainties due to possible errors in the origin times, but the

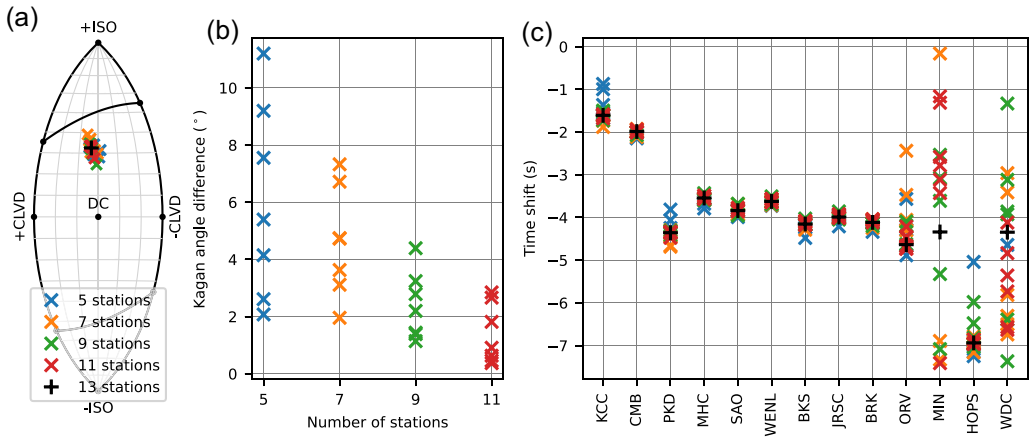

Figure 7. Solutions for event 1997/11/22 17:20:35 recovered using 28 random station subsets. The subset size colour codes are shown in the legend in panel (a). (a) On a lune diagram (Tape & Tape 2012), colour crosses plot the recovered moment tensors (MT) from all subset realizations, and the black plus mark the reference solution recovered with all 13 stations (shown in Fig. 6). (b) The crosses plot the Kagan (1991) angles, the smallest angle to match the double couple (DC) parts of two MTs, between the subset realizations' and the reference MT. (C) The colour crosses and black plus plot station-specific time-shifts recovered in the inversions of all station subsets.

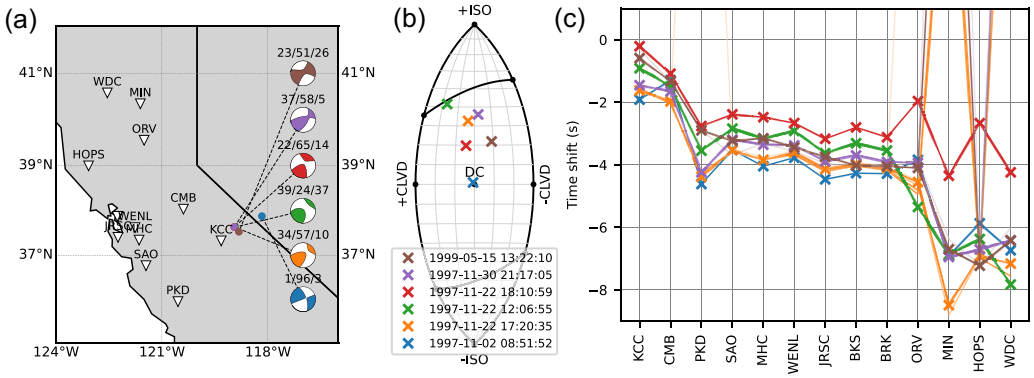

Figure 8. Robust trend in recovered station-specific time-shifts for six earthquake in the Long Valley Caldera region. The event colour codes in the legend of panel (b) apply to all figure panels. (a) Location map of six events analysed in this experiment. The beach balls plot this study's MT solutions. (b) Crosses plot the solutions on a lune diagram (Tape & Tape 2012). (c) Thin colour lines plot the time-shift variation of 48 selected inversion runs (out of 96 trials), and the crosses mark the trend of their median values.

decreasing trend is consistent. Assuming that the crustal and uppermost mantle structures are generally homogenous, the decreasing trend could suggest that the SoCal model is slightly faster than the local Earth structure (see Fig. 5c).

5 DISCUSSION

In summary, we have presented the details of an efficient gradient-based method and demonstrated its feasibility, robustness and scalability to jointly invert MT parameters, centroid depth and station-specific time-shifts through numerical experiments and real data examples. In the following, we discuss some inherent limitations of the proposed algorithm, our measures to mitigate the limitations and thoughts on the way forward.

In the current implementation, we use linear interpolation (eq. 5) of GFs pre-computed on regular depth grids to define a continuous and differentiable loss function with centroid depth (eq. 9). The interpolation approach can be extended to consider unknown 3-D hypocentral coordinates without significantly affecting the design of the inversion algorithm. Translating the existing forward methods (e.g. Herrmann 2013) into a modern programming framework where autodifferentiation functionality is supported, for example *TensorFlow* or *PyTorch*, could be a promising way to incorporate the source location into the present inversion framework. However, the computation cost is expected to increase when more spatial variables are introduced into the inversion.

It is worth noting that the pointwise L_2^2 misfit function (eqs 6 and 9) assumes uncorrelated data noise in the observation. Recent studies demonstrate the benefit of considering correlated noise characterized by symmetric covariance matrices, which can be estimated either from ambient noise (Duputel *et al.* 2012; Mustać & Tkalčić 2016; Vackář *et al.* 2017) or involve the prior assumptions of Earth's structural error (Phạm & Tkalčić 2021; Vasyura-Bathke *et al.* 2021). Incorporating the covariance matrices into this study's proposed algorithm is practical, but its robustness is subject to further investigation. Similarly, it is feasible, but yet to be verified, to incorporate an unknown source–time function (STF), representing the history of realizing energy rather than an impulse source in time, when the STF is represented as a weighted linear combination of several bases (Stähler & Sigloch 2014).

Because the proposed joint inversion is cast in the optimization framework, it does not benefit from non-linear parametrization

methods featuring a homogeneous distribution of MTs on the parameter space (Stähler & Sigloch 2014; Tape & Tape 2015). Instead, we chose the primitive MT parametrization (eq. 1) in this work so the derivatives to MT parameters can be calculated rapidly (eq. 10). For the same reason, we expect the implementation's performance to be similar when using other linear MT parametrization methods (e.g. Kikuchi & Kanamori 1982; Kawakatsu 1996), which are convenient when full MT is not required, for example, deviatoric MT (e.g. Hejrani *et al.* 2017; Hejrani & Tkalčić 2018).

The use of the L_2^2-misfit function between predicted and observed waveforms could pose a concern regarding the presence of local minima, most likely due to the waveform cycle-skipping (Sambridge *et al.* 2022). Thanks to the proposed inversion's efficiency, this study selects solutions converged from diverse initializations to minimize the risk of a local minimum solution. Using novel waveform similarity measurements, which are not subjected to local minima, such as the Warsterstein distance (Sambridge *et al.* 2022), could be an interesting future research topic for this application.

The main limitation of the presented method in an optimization framework is the lack of sufficient uncertainty estimates concerning inverted solutions because it only outputs the optimal solution. This is of critical importance when applying to highly non-unique settings such as critically shallow earthquakes or explosions (Kawakatsu 1996; Ford *et al.* 2010; Alvizuri & Tape 2018; Hejrani & Tkalčić 2020; Hu *et al.* 2023). To circumvent this limitation, we appraise the solution and its uncertainty from a subset of best-fitting solutions obtained by repeating the inversions multiple times. A holistic approach to obtain the complete posterior distribution of the inverted parameters is to investigate effective gradient-based Hamiltonian Monte Carlo sampler (Fichtner & Simutė 2018), thanks to the availability of the loss function's derivatives.

6 CONCLUSION

In conclusion, we present a gradient-based inversion method in an optimization framework for a classical problem in regional MT inversion, the joint inversion of MT parameters, centroid depth and station-specific time-shifts. The station-specific time-shifts can be considered a simplified proxy for 3-D Earth structure errors with incomplete GFs in MT inversion problems. To incorporate centroid depth in the inversion, we interpolate GFs at an arbitrary depth from pre-computed GFs at regular depth grids. In doing so, the L_2^2 misfit function between the prediction and shifted observation is cast in the frequency domain thanks to Parseval's theorem. Tests on controlled synthetic experiments and data from pilot events from the Long Valley Caldera region demonstrated the proposed method's feasibility, robustness and scalability. This paper hopes to highlight a fresh opportunity to benefit from the computational infrastructures thanks to the rapidly growing artificial intelligence communities for geophysical problems.

ACKNOWLEDGMENTS

This work greatly benefited from discussion with Jinyin Hu and Hrvoje Tkalčić through ongoing research on MT inversion. The Air Force Research Laboratory's grant, contract number FA9453-20-C-0072, supported the author's *post doc* at The Australian National University. He also acknowledges financial support from the Australian Research Council through a Discovery Early Career Researcher Award, project DE230100025. This research was undertaken with the assistance of resources from the National Computational Infrastructure (NCI Australia), an NCRIS enabled capacity supported by the Australian Government. The author thanks Editor Carl Tape, Jiří Vackář and an anonymous reviewer for constructive review comments, which significantly improve the quality of the this paper.

AUTHOR CONTRIBUTIONS

Conceptualization, data curation, formal analysis, funding acquisition, investigation, methodology, project administration, resources, software, validation, visualization, writing – original draft and writing – review and editing were all done by author Thanh-Son Phạm.

SUPPORTING INFORMATION

Supplementary data are available at *GJI* online.

Figure S1. Summary of inversion results for a numerical experiment using data computed by a correct earth model, that is $k = 0$ per cent. The centroid depth is fixed at 10 km. (a) Location map of the event and monitoring stations. The black and red beach balls show the deviatoric moment tensors (MT) of the actual input and the recovered solution. (b) The input MT (black plus) and the recovered MT (red cross) are denoted on a lune diagram of source types (Tape & Tape 2012). (c) Black lines show the evolution of descending losses (eq. 9 in the main text) as a function of epochs for 48 solutions that produced the smallest losses out of the 96 independent runs. The grey lines show the corresponding evolution of the event-depth parameter. The text denotes the forward earth model, model error magnitude, recovered event depth, moment magnitude and standard decomposition of isotropic (ISO), double couple (DC) and compensated linear vector dipole (CLVD) components. (d) Synthetic data and 48 best-predicted waveforms are shown in black and red, respectively. The right-hand panel shows the output station-specific Gme shifts and estimated uncertainties.

Figure S2. Summary of inversion results for synthetic data computed with $k = -1$ per cent model error. Other details are the same as in Fig. S1.

Figure S3. Summary of inversion results for synthetic data computed with $k = 1$ per cent model error. Other details are the same as in Fig. S1.

Figure S4. Summary of inversion results for synthetic data computed with $k = 3$ per cent model error. Other details are the same as in Fig. S1.

Figure S5. Summary of inversion results for synthetic data computed with $k = -5$ per cent model error. Other details are the same as in Fig. S1.

Figure S6. Summary of inversion results for synthetic data computed with $k = 5$ per cent model error. Other details are the same as in Fig. S1.

Figure S7. Summary of inversion results for real data computed from 1997-11-02 08:51:52 event catalogued in the North California Earthquake Data Center. Other details are the same as in Fig. S1.

Figure S8. Summary of inversion results for real data computed from 1997-11-22 12:06:55 event catalogued in the North California Earthquake Data Center. Other details are the same as in Fig. S1.

Figure S9. Summary of inversion results for real data computed from 1997-11-22 18:10:59 event catalogued in the North California Earthquake Data Center. Other details are the same as in Fig. S1.

Figure S10. Summary of inversion results for real data computed from 1997-11-30 21:17:05 event catalogued in the North California Earthquake Data Center. Other details are the same as in Fig. S1.
Figure S11. Summary of inversion results for real data computed from 1999-05-15 13:22:10 event catalogued in the North California Earthquake Data Center. Other details are the same as in Fig. S1.

Please note: Oxford University Press is not responsible for the content or functionality of any supporting materials supplied by the authors. Any queries (other than missing material) should be directed to the corresponding author for the paper.

DATA AND CODE AVAILABILITY

Data for this study come from the Berkeley Digital Seismic Network (BDSN), doi:10.7932/BDSN, operated by the UC Berkeley Seismological Laboratory, which is archived at the Northern California Earthquake Data Center (NCEDC), doi:10.7932/NCEDC. Source files to reproduce the data analysis and figures presented in this paper is available at: https://github.com/tsonpham/JointMTS.git.

REFERENCES

Aki, K. & Richards, P.G., 2002. *Quantitative Seismology,* 2nd edn, University Science Books.

Alvizuri, C. & Tape, C., 2018. Full moment tensor analysis of nuclear explosions in North Korea, *Seismol. Res. Lett.,* **89,** 2139–2151.

Del Moral, P., Doucet, A. & Jasra, A., 2006. Sequential Monte Carlo samplers, *J. R. Stat. Soc., B: Stat. Methodol.,* **68,** 411–436.

Dreger, D.S. & Helmberger, D.V., 1990. Broadband modelling of local earthquakes, *Bull. seism. Soc. Am.,* **80,** 1162–1179.

Dreger, D.S., Tkalčić, H. & Johnston, M., 2000. Dilational processes accompanying earthquakes in the Long Valley Caldera, *Science,* **288,** 122–125.

Duputel, Z., Rivera, L., Fukahata, Y. & Kanamori, H., 2012. Uncertainty estimations for seismic source inversions, *Geophys. J. Int.,* **190,** 1243–1256.

Dziewonski, A.M., Chou, T.-A. & Woodhouse, J.H., 1981. Determination of earthquake source parameters from waveform data for studies of global and regional seismicity, *J. geophys. Res.,* **86,** 2825–2852.

Fichtner, A. & Simutė, S., 2018. Hamiltonian Monte Carlo inversion of seismic sources in complex Media, *J. geophys. Res.,* **123,** 2984–2999.

Ford, S.R., Dreger, D.S. & Walter, W.R., 2010. Network sensitivity solutions for regional moment-tensor InversionsNetwork sensitivity solutions for regional moment-tensor inversions, *Bull. seism. Soc. Am.,* **100,** 1962–1970.

Goodman, J. & Weare, J., 2010. Ensemble samplers with affine invariance, *Commun. Appl. Math. Comput. Sci.,* **5,** 65–80.

Gradshteyn, I.S., Ryzhik, I.M., Jeffrey, A. & Zwillinger, D., 2000. *Table of Integrals, Series, and Products,* 6th edn, Academic Press.

Hejrani, B. & Tkalčić, H., 2018. The 20 May 2016 Petermann Ranges earthquake: centroid location, magnitude and focal mechanism from full waveform modelling, *Aust. J. Earth Sci.,* **66**(1), 37–45.

Hejrani, B. & Tkalčić, H., 2020. Resolvability of the centroid-moment-tensors for shallow seismic sources and improvements from modeling high-frequency waveforms, *J. geophys. Res.,* **125,** e2020JB019643, doi:10.1029/2020JB019643.

Hejrani, B., Tkalčić, H. & Fichtner, A., 2017. Centroid moment tensor catalogue using a 3-D continental scale earth model: application to earthquakes in Papua New Guinea and the Solomon Islands, *J. geophys. Res.,* **122,** 5517–5543.

Herrmann, R.B., 2013. Computer Programs in seismology: an evolving tool for instruction and research, *Seismol. Res. Lett.,* **84,** 1081–1088.

Hu, J., Phạm, T.-S. & Tkalčić, H., 2023. Seismic moment tensor inversion with theory errors from 2D earth structure: implications for the 2009-2017 DPRK nuclear blasts, *Geophys. J. Int.,* **235,** doi:10.1093/gji/ggad348.

Jost, M.L. & Herrmann, R.B., 1989. A student's guide to and review of moment tensors, *Seismol. Res. Lett.,* **60,** 37–57.

Kagan, Y.Y., 1991. 3-D rotation of double-couple earthquake sources, *Geophys. J. Int.,* **106,** 709–716.

Kawakatsu, H., 1996. Observability of the isotropic component of a moment tensor, *Geophys. J. Int.,* **126,** 525–544.

Kikuchi, M. & Kanamori, H., 1982. Inversion of complex body waves, *Bull. seism. Soc. Am.,* **72,** 491–506.

Kingma, D.P. & Ba, J., 2014. Adam: a method for stochastic optimization, arXiv E-Prints. https://doi.org/10.48550/arXiv.1412.6980.

Kühn, D., Heimann, S., Isken, M.P., Ruigrok, E. & Dost, B., 2020. Probabilistic moment tensor inversion for hydrocarbon-induced seismicity in the Groningen Gas Field, the Netherlands, part 1: testing, *Bull. seism. Soc. Am.,* **110,** 2095–2111.

Minson, S.E. & Dreger, D.S., 2008. Stable inversions for complete moment tensors, *Geophys. J. Int.,* **174,** 585–592.

Mustać, M. & Tkalčić, H., 2016. Point source moment tensor inversion through a Bayesian hierarchical model, *Geophys. J. Int.,* **204,** 311–323.

Nooshiri, N., Bean, C.J., Dahm, T., Grigoli, F., Kristjánsdóttir, S., Obermann, A. & Wiemer, S., 2022. A multibranch, multitarget neural network for rapid point-source inversion in a microseismic environment: examples from the Hengill Geothermal Field, Iceland, *Geophys. J. Int.,* **229,** 999–1016.

Petersen, G.M., Cesca, S., Heimann, S., Niemz, P., Dahm, T., Kühn, D., Kummerow, J. & Plenefisch, T.& the AlpArray and AlpArray-Swath-D working groups, 2021. Regional centroid moment tensor inversion of small to moderate earthquakes in the Alps using the dense AlpArray seismic network: challenges and seismotectonic insights, *Solid Earth,* **12,** 1233–1257.

Phạm, T.-S. & Tkalčić, H., 2021. Toward improving point-source moment-tensor inference by incorporating 1D earth model's uncertainty: implications for the Long Valley caldera earthquakes, *J. geophys. Res.,* **126,** 2021JB022477,.

Roberts, G.O. & Rosenthal, J.S., 2001. Optimal scaling for various metropolis-Hastings algorithms, *Stat. Sci.,* **16,** 351–367.

Sambridge, M., Jackson, A. & Valentine, A.P., 2022. Geophysical inversion and optimal transport, *Geophys. J. Int.,* **231,** doi:10.1093/gji/ggac151.

Silwal, V. & Tape, C., 2016. Seismic moment tensors and estimated uncertainties in southern Alaska, *J. geophys. Res.,* **121,** 2772–2797.

Simutė, S., Boehm, C., Krischer, L., Gokhberg, A., Vallée, M. & Fichtner, A., 2023. Bayesian seismic source inversion with a 3-D earth model of the Japanese islands, *J. geophys. Res.,* **128,** e2022JB024231, doi:10.1029/2022JB024231.

Stähler, S.C. & Sigloch, K., 2014. Fully probabilistic seismic source inversion—part 1: efficient parameterisation, *Solid Earth,* **5,** 1055–1069.

Stein, S. & Wysession, M., 2003. *An Introduction to Seismology, Earthquakes, and Earth Structure,* 1 edn, Blackwell Publishing.

Steinberg, A., Vasyura-Bathke, H., Gaebler, P., Ohrnberger, M. & Ceranna, L., 2021. Estimation of seismic moment tensors using variational inference machine learning, *J. geophys. Res.,* **126,** e2021JB022685, doi:10.1029/2021JB022685.

Tape, W. & Tape, C., 2012. A geometric setting for moment tensors, *Geophys. J. Int.,* **190,** 476–498.

Tape, W. & Tape, C., 2015. A uniform parametrization of moment tensors, *Geophys. J. Int.,* **202,** 2074–2081.

Thurin, J. & Tape, C., 2023. Comparison of force and moment tensor estimations of subevents during the 2022 Hunga–Tonga submarine volcanic eruption, *Geophys. J. Int.,* **235,** 1959–1981.

Thurin, J., Tape, C. & Modrak, R., 2022. Multi-event explosive seismic source for the 2022 Mw 6.3 Hunga Tonga submarine volcanic eruption, *Seism. Rec.,* **2,** 217–226.

Vackář, J., Burjánek, J., Gallovič, F., Zahradník, J. & Clinton, J., 2017. Bayesian ISOLA: new tool for automated centroid moment tensor inversion, *Geophys. J. Int.,* **210,** 693–705.

Vasyura-Bathke, H., Dettmer, J., Dutta, R., Mai, P.M. & Jónsson, S., 2021. Accounting for theory errors with empirical bayesian noise models in

nonlinear centroid moment tensor estimation, *Geophys. J. Int.,* **225,** 1412–1431.

Vasyura-Bathke, H. *et al.*, 2020. The Bayesian earthquake analysis tool, *Seismol. Res. Lett.,* **91,** 1003–1018.

Viltres, R., Nobile, A., Vasyura-Bathke, H., Trippanera, D., Xu, W. & Jónsson, S., 2021. Transtensional rupture within a diffuse plate boundary zone during the 2020 Mw 6.4 Puerto Rico earthquake, *Seismol. Res. Lett.,* **93,** 567–583.

Zhao, L.-S. & Helmberger, D.V., 1994. Source estimation from broadband regional seismograms, *Bull. seism. Soc. Am.,* **84,** 91–104.

Zhu, L. & Ben-Zion, Y., 2013. Parametrization of general seismic potency and moment tensors for source inversion of seismic waveform data, *Geophys. J. Int.,* **194**(2), 839–843.

Zhu, L. & Helmberger, D.V., 1996. Advancement in source estimation techniques using broadband regional seismograms, *Bull. seism. Soc. Am.,* **86,** 1634–1641.